Low-cost, high-resolution and no-manning distributed sensing system for the continuous monitoring of fruit growth in precision farming

Lorenzo Mistral Peppi[1], Matteo Zauli[1], Luigi Manfrini[2], Luca Corelli Grappadelli[2], Luca De Marchi[1], Pier Andrea Traverso[1]

[1] DEI - Department of Electrical, Electronic and Information Engineering "Guglielmo Marconi", University of Bologna, 40136 Bologna, Italy
[2] DISTAL - Department of Agricultural and Food Science, University of Bologna, University of Bologna, 40127 Bologna, Italy

ABSTRACT

Accurate, continuous and reliable data gathering and recording about crop growth and state of health, by means of a network of autonomous sensor nodes that require minimal management by the farmer will be essential in future Precision Agriculture.
In this paper, a low-cost multi-channel sensor-node architecture is proposed for the distributed monitoring of fruit growth throughout the entire ripening season. The prototype presented is equipped with five independent sensing elements that can be attached each to a sample fruit at the beginning of the season and are capable of estimating the fruit diameter from the first formation up to the harvest. The sensor-node is provided with a LoRa transceiver for wireless communication with the decision making central, is energetically autonomous thanks to a dedicated energy harvester and an accurate design of power consumption, and each measuring channel provides sub-mm 9.0-ENOB effective resolution with a full-scale range of 12 cm. The accurate calibration procedure of the sensor-node and its elements is described in the paper, which allows for the compensation of temperature dispersion, noise and non-linearities. The prototype was tested on field in real application, in the framework of the research activity for next-generation Precision Farming performed at the experimental farm of the Department of Agricultural and Food Science of the University of Bologna, Cadriano, Italy.

1. INTRODUCTION

The rise of new technologies makes possible to approach classical issues with modern, smart solutions. Agriculture is definitely benefiting from these innovations: quick global development, population growth, climate change and a new awareness of food, its safety and the impact its production has on the environment have led to terms such as "Precision Farming", "Digital Farming" or "Agriculture 4.0" becoming more and more widespread and considered as a real added value to the agricultural product.

The term Precision Agriculture (PA) encompasses many disciplines and technologies employed: artificial intelligence, autonomous control of agricultural equipment, automatic decision-making systems, quality control and application of treatments by drones, and so on, in order to increase productivity and environmental quality [1].

The key element, therefore, is the ability to acquire, transmit and process information in order to monitor crops, to make autonomous decisions through decision-support systems (DSS) (as an example see [2]) and/or to provide data about a particular situation in order to allow for a decision to be made that is as correct and spatially and temporally customised as possible [1], [3]. The advent of IoT [4] networks has further increased the pervasiveness of in-field sensing due to the possibility, particularly through LoRaWan networks, to cover large areas

using extremely low-power, adequate reliability and low-cost hardware [5], [6]. In addition, smart devices allow farmers to be employed for different tasks, for which human presence is essential, reducing the need for human intervention and therefore lowering overall farm operating costs.

However, farmers often perceive new technologies more as a complication than an advantage, mainly because of their inexperience, the lack of interoperability between various technologies, the complexity, the often very high costs, and the inability to handle such large amounts of data [7], [8]. Consequently, efforts must be made to make these technologies easy for the farmer to install, understand, successfully exploit, and maintain.

The monitoring of fruit growth does not only help to estimate the yield [9], [10] but also provides additional information, such as the water stress status of the plants [11], [12]. In addition, by comparing the data acquired in real time with predictive growth models, corrective actions can be taken in the orchard.

The most common techniques for measuring fruit dimension employ LVDT (Linear Variable Displacement Transducer) sensors and strain gauges or potentiometers [13], [14] which, despite being highly accurate, are limited by a usually very small measurable range. Therefore, in order to keep on with the measurement process, frequent re-positioning of the sensor on the fruit is required. This time- and labour- consuming activity has a cost, and therefore an impact on farmer's income. There are alternative solutions that do not require relocation over time, such as those employing optical sensors directly on the fruit, as in [15], but they are usually affected by low accuracy and the inability to detect fruit shrinkage. Currently, systems capable of agricultural analysis have been developed using computer vision [16] and artificial intelligence methodologies [17]. In particular, techniques to estimate the number of fruits and their size [18], [19], [20], [21], [22] have been introduced. However, the accuracy achievable by these devices is still low compared to traditional techniques.

This work aims to present the design, implementation and experimental assessment of a low-cost multi-channel distributed sensing system, aimed at the high-resolution, continuous estimation and recording of the diameter of fruits directly on the tree throughout the whole growth process. The system is non-invasive and does not either damage or warp the fruits, is energetically autonomous and is strongly uninfluenced by environmental conditions. Relocation of sensing elements is not needed either during the ripening season, as required by the sensors used so far because of their small measurable range, thanks to an adequate full-scale range that is greater than the size of the fruit (e.g., apple, orange) once it has reached the typical ripe dimension.

In comparison with the preliminary work presented in [23], in which a first, single-channel basic prototype was shown to illustrate the concept, a complete multi-channel sensor-node solution is presented here, with also the addition of an energy harvesting section able to guarantee season-long autonomous operation and a LoRa transceiver to allow data communication even at far distance from the receiving gateway. The full calibration of the multi-channel system was refined and is described step-by-step in details. Two in-field measurement campaigns are also presented, carried out at an apple orchard at the experimental farm of the Department of Agricultural and Food Science of Bologna, Cadriano, Italy.

The paper is organized as follows. In Section 2 the operating principle of the device is explained, and system architecture is
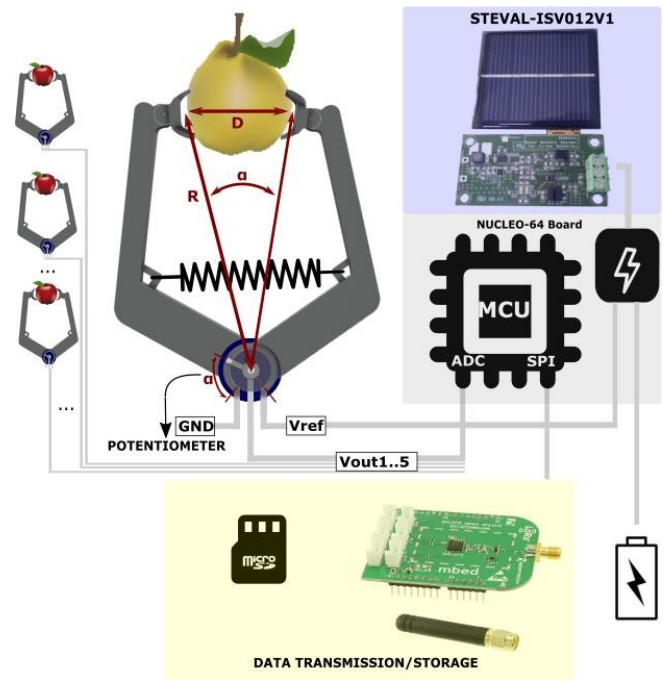

Figure 1. Architecture of the sensor-node, with details of one of the five sensing elements.

shown. In Section 3 all the main components of the multi-channel sensor-node are described in details, with particular emphasis to the architectural/design solutions exploited to maximize final reliability and accuracy. Section 4 describes the refined full calibration procedure of the prototype. Finally, in Section 5 results of in-field tests, conducted on an apple orchard, are shown.

2. SYSTEM ARCHITECTURE AND OPERATING PRINCIPLE

Unlike the conventional methods proposed in literature, where the growth of the fruit determines a stimulus directly detected by a sensitive element (potentiometer, LVDT, etc.), in this application the i-th sensing element (i.e., the front-end of the i-th measuring channel) is made of a structure of known dimensions. The structure is composed of two solid arms bounded together at one end with a bold (Figure 1 for a five-channel sensor-node). It is used to interface the object to be measured to the element itself. The plier is kept in place by means of a spring while a reference voltage-supplied (V_{ref}) potentiometer, which is placed within the fulcrum of the plier and is rigidly connected to one of the two arms of the clamp, converts the opening angle α into a voltage acquired by the Analog-to-Digital Converter (ADC) integrated into the micro-controller unit (MCU) governing the overall node. The voltage at the output of each sensing element is proportional to the opening angle of the clamp, since the partition ratio of the potentiometer is directly proportional to α, and the linear width d that represents the measurand is indirectly obtained from the A/D acquired voltage according to (1):

$$d = 2\,R \cdot \cos\left(\frac{\pi}{2} - \frac{\alpha(V_{out})}{2}\right). \tag{1}$$

The task of the MCU is to trigger readings, to perform all the in-site calibration and compensation processes on the acquired raw data and to manage storage and/or wireless transmission of data about the fruit growth evolution to a remote decisional unit.
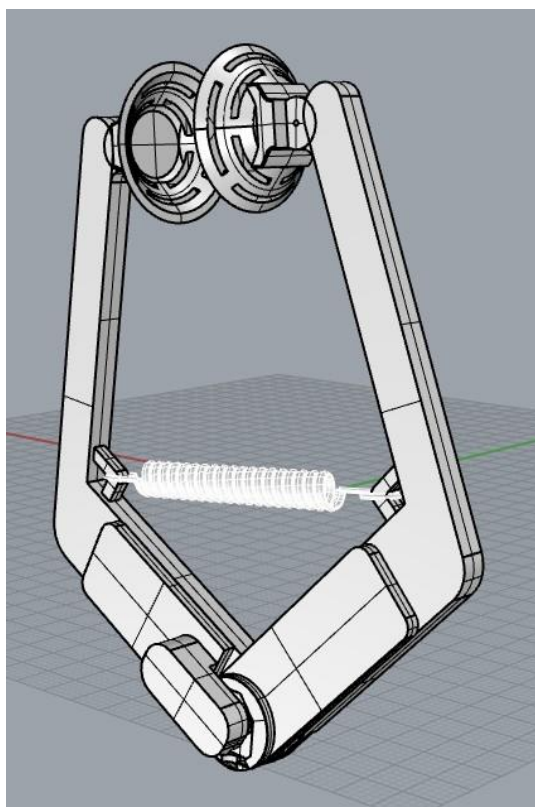
Figure 2. 3D rendering of the plier designed for the realization of each sensing element.

In addition, the MCU also manages the power supply timing of potentiometers, ensuring minimum power consumption of the entire sensor-node.

3. SENSOR-NODE PROTOTYPE

In this Section, the main components that were exploited in the realization of a prototype for a complete five-sensing element sensor-node will be described, together with their characteristics and related design strategies.

3.1. ABS Pliers

The plier in each sensing element consists of two arms, which are bolted together. A rotary potentiometer is located in a recess within the pivot, to sense the opening angle α between the two arms. The plier acts as an adapter to allow to easily optimize the full-scale for the width d during the design phase, while preserving the same angular full-scale. More precisely, to vary the maximum measurable distance d_{FS}, given the same maximum opening angle, it is only necessary to re-scale the effective length R of the plier arms.

After preliminary tests with different materials, the plier was manufactured using Acrylonitrile Butadiene Styrene (ABS), through a 3D printing process. The use of ABS makes it possible to obtain a structure that is robust but at the same time light-weighted: in fact, the warping of fruits due to an excessively heavy plier, which would lead to a distorted estimated growth profile, must be avoided at all costs.

In order to avoid any interference with the growth of the fruit, a "half horseshoe" shape (shown in Figure 2) was chosen for the arms, while the mechanical elements that rest on the fruit are cup-shaped to increase the contact surface, their edges being coated with silicone to prevent slipping. On the side of the cups,

slits are located to prevent the accumulation of moisture and the consequent possible development of fungal diseases. The dimensional parameters of the plier are necessarily customized according to the species of fruit, in order to allow for the capability of monitoring the entire ripening process, optimize the nominal resolution and maximize the overall accuracy of each channel. The size of these prototype calipers is such as to allow for the monitoring of apple growth, therefore they have been designed to offer a full-scale range of d_{FS} = 12 cm, starting from the requirement of a maximum opening angle of α_{FS} = 60 deg (see below), which resulted in an effective length R = 12 cm.

3.2. Angular sensor

As angular sensor, a single turn potentiometer with an electrical angle of 60 deg was chosen. The potentiometer, connected as a voltage divider, is supplied by a reference voltage V_{ref} shared with the ADC V_{ref} in order to minimize gain errors. In such a configuration the output voltage V_{out} of the sensing element is proportional to the opening angle, and thus algebraically related to the measurand d according to (1).

The PHS11-1DBR10KE60 [24], from TT Electronics, was the commercial component adopted. Although tests conducted over a period of months have not shown any particular weathering issues for the potentiometer, in order to protect from dust, dirt and moisture it was coated with a layer of water-resistant insulating grease.

3.3. MCU, ADC and temperature sensor

For this application a microcontroller with low power consumption and integrated A/D channels was required. At first CMWX1ZZABZ-091 Murata modules were selected. This device integrates, together with an STM32L072 MCU, a Semtech SX1272 LoRa transceiver, freeing the designer from problems related to the management of RF circuits. However, components supply shortage related to the 2020-22 pandemic forced the use of a STMicroelectronics NUCLEO64 demo board [25] equipped with a STM32L152RE MCU, whose power supply circuit was exploited and whose pin headers were used as interface to the five potentiometers and the SD card for local data storage. The MCU can be easily integrated with a LoRa module (e.g., MBED SX1272MB2DAS) as well. STM32L152RE is a 32-bit microprocessor incorporating a 12-bit successive-approximation ADC, SPI and I2C peripherals, and featuring low power modes [26].

As already mentioned, thanks to the presence of PMOS devices acting as power switches, the same reference voltage used by the A/D stage was employed to supply each potentiometer: in this way it was possible to take advantage of the entire full-scale range of the ADC and, at the same time, compensate for both short- and long-time dispersion effects of the reference voltage. By adopting 3.3 V as V_{ref}, the nominal quantization step of the ADC is 806 μV, which is approximately equivalent to a nominal resolution of 30 μm for each sensing channel.

The MCU makes internally available a temperature sensor, which was used for thermal compensation in the framework of the real-time overall calibration procedure (Section 4) implemented for each channel. During the production of the MCU this sensor is calibrated, and calibration coefficients made available within read-only portions of the memory [26]. Nonetheless, a comparison was made for performance assessment between this sensor and a reference one (namely, HTS221 from STMicroelectronics) characterised by an accuracy of 1.0 °C in the 0 °C to 60 °C range [27]. The maximum

estimated deviation between the two sensors in the 24 °C to 72 °C range was 1.34 °C, which allowed to consider the accuracy of the internal MCU sensor adequate enough for the thermal compensation cited above.

3.4. Power supply

The voltage provided by the battery and harvester (see next Subsections) had to be adjusted down to 3.3 V, which is a compatible level with the operation of the MCU and peripherals. To this aim, the LD39050PU33R LDO from STMicroelectronics available in the Nucleo board has been used, which allows for a stable, low-noise power supply. This device is characterized by very good performance in terms of output voltage noise (30 µV$_{rms}$ over 10 Hz to 100 kHz bandwidth) and thermal stability [28]. In order to switch off the supply to potentiometers and to SD card, when not in use, PMOSs acting as switches are used, as described in Subsection 3.7.

3.5. Data storage and communication

The LoRa transmitter uses an MBED SX1272MB2DAS [29] demoboard, fitted with a Semtech SX1272 [30] transceiver. All RF-related circuitry is relegated to this board, which is connected to the NUCLEO64 via a set of Arduino-compatible connectors. The SX1272 transceiver is designed to operate in the 868 MHz frequency band, and it communicates with the microcontroller via an SPI interface [30]. In addition, DIO lines are used by the Semtech LoRaMac.node stack to interface with the transceiver. The power supply line of this board is connected directly to the Nucleo board to exploit the power supply stage of the latter.

As an alternative to sending data over the air, these can be saved locally by means of an SD Card (Figure 1).

3.6. Energy harvester

To ensure maintenance-free operation of the sensor- node during the entire fruit growth period, it is essential to rely on a low-cost source of energy that does not run out in a short interval of time. By considering consumption estimates and planned duty cycles, it is possible to determine the most suitable energy source to ensure high system autonomy.

A single acquisition cycle, consisting of interrogating all five sensing elements every 600 s, processing and storing of data on
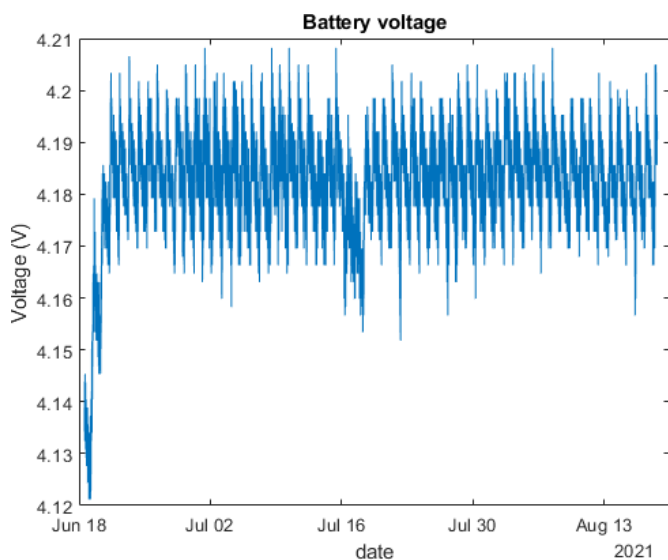

Figure 3. Battery voltage of the energy harvester during open field tests. It is worth noting that the battery is always fully charged, and even during bad weather days no significant battery discharge is noticeable.

the SD card (local storage is considered in the following discussion), requires a total of 1.63 J, such estimation being performed by averaging data from different SD Card manufacturers [31].

As an example, with a 500 mAh battery the operating time of the prototype would be around 25 days, without taking into account self-discharge phenomena, while for many fruit species the growth and ripening times are much longer [9], [32]. Therefore, such a local battery is not suitable for a virtually maintenance-free node. Increasing the battery capacity is not practical, either: at the beginning of the season all the batteries should be charged, and if the number of nodes is high many chargers would be needed, which could be a significant cost, because of their price and required manpower, even if wireless power transfer was used, such as in [33]. For this reason, the adoption of a photovoltaic harvesting sub-system, with a small rechargeable back-up battery, was considered as the optimal solution. This avoids the use of external chargers or non-rechargeable batteries, which are by their nature also a major source of pollution. As it will be described in the following, when the photovoltaic panel is exposed to full sunlight it is possible to keep the back-up battery fully charged. However, in the case of indirect exposure to light, such as in greenhouses applications, recovery of the energy consumed by the sensor-node is not always guaranteed. For this reason, the battery voltage level is monitored and forwarded every time a data transmission takes place.

For the prototype a STEVAL-ISV012V1 evaluation board from ST Microelectronics was used. Included in the evaluation board are a 400 mW$_{peak}$ photovoltaic panel, namely SZGD6060-4P from NBSZGD, a SPV1040 step-up converter with MPPT (Maximum Power Point Tracker) and a L6924D charge controller for Li-Ion batteries, both from STMicroelectronics [34]. The use of a step-up converter with MPPT algorithm allows to continuously track output voltage and current of the solar cell and therefore allows to maintain its maximum power point while changing lighting and load conditions, thus maximizing the harvested energy and increasing the overall efficiency of the stage.

Tests carried out in open field, at the farm of the Faculty of Agriculture of University of Bologna (Cadriano, Bologna) between June and August 2021, have shown how this solution is able to ensure a sufficient power supply to power the prototype when used outdoor: the harvester is able to keep the battery fully charged during the day, while during the night the discharge is minimal, as it is possible to appreciate in Figure 3. It is worth noting that the test was carried out in rows protected by rain-hail nets and the photovoltaic panel oriented in the east direction.

3.7. Power gating

When a measurement is performed, the potentiometers are powered by a reference voltage. Without power gating systems, the energy wasted during quiescent operation would be much higher than the one needed to keep the MCU in stand-by: a current of 330 µA would flow continuously in each one of the 5 potentiometers, and the overall consumption would not be negligible.

To implement the power gating function PMOS devices are used: a low logic value to the Gate pin allows the PMOS to start conducting, powering the potentiometers. By using a PMOS, it is not required to force a high logic value to the Gate to keep the load disconnected: by using this configuration I/O interfaces of the MCU can be disabled, thus saving energy and leaving the
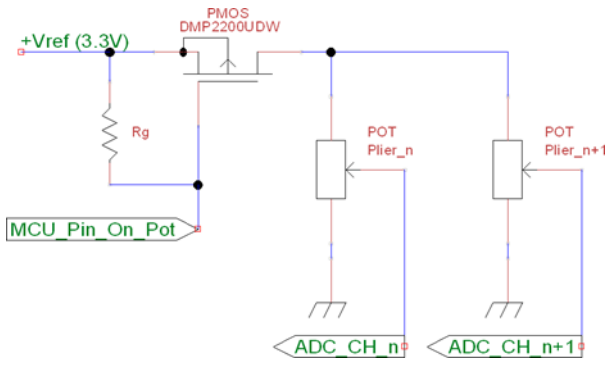
Figure 4. Schematic of PMOS switch stage.

GPIO pins floating while allowing potentiometers to be not powered. This is due to the fact that, by inserting a resistor Rg (Figure 4) of appropriate value between Gate and Source, the device will always remain off as $VGS = V_{\text{Rg}} \approx 0$ V because $I_{\text{Gate}} \approx 0$ V. Even a high value of R_g keeps the device off and allows, when $VGS < 0$ V or when the PMOS is conducting, to dissipate over Rg a negligible amount of energy.

A key factor in the choice of MOS is the low R_{dson} of the device: the lower its value, the lower the influence of this parameter on the final measurement. This aspect will be discussed in more detail in Sec. 4.2 .

The commercial device chosen is DMP2200UDW PMOS, from Diodes Incorporated. This device has two extremely low resistivity [35] (Spice simulations show a resistivity of 207 mΩ at 27.5 °C in actual operative point) PMOS placed within the same package. Each MOS is used to activate two potentiometers at a time: in this way, it is possible to power only those potentiometers whose output must be activated, thus resulting in an overall lower power consumption.

4. REAL-TIME CALIBRATION PROCEDURE

Several sources of uncertainty, mainly related to the variations of temperature in which the system will operate, have been identified in the uncalibrated prototype. In an open field or greenhouse, at least a temperature range of a few tens of degrees has to be considered. Furthermore, this system must be able to operate in the most varied conditions, in direct sunlight and during all months of the year. Therefore, temperature stability is

essential and temperature dispersion must be carefully compensated. In addition, the real-time calibration procedure described in Subsections 4.2, 4.3 and 4.4 and implemented in the prototype compensates also for short-term instability (e.g., noise) and non-linearities affecting each sensing channel (Figure 5).

4.1. A/D acquisitions and data averaging

For a given sensing channel, in order to obtain a single fruit size reading the ADC is activated in continuous mode every 600 s to acquire M sequences of N samples each of the voltage V_{out} at the output of the potentiometer in the channel. A $\overline{V}_R$ estimator is then computed as the averaging of the $M \cdot N$ samples $V_{R,n}^{(m)}$ where (m, n) denote the $m-th$ sequence and the $n-th$ sample in the sequence, respectively:

$$\overline{V}_R = \frac{1}{M \cdot N} \sum_{m=1}^{M} \sum_{n=1}^{N} V_{R,n}^{(m)} . \tag{2}$$

The estimator in (2) could be used directly as the V_{out} value in (1) to compensate for short-term instabilities (mainly noise) in the A/D conversion process. However, the procedure would not take into account thermal dispersion and non-linearities, thus additional correction steps were implemented, as discussed in the next Subsections.

A trade-off between accuracy in rejecting short- term instability and power consumption needs to be considered when choosing the values of N, M and the sampling period. Indeed, the higher the number of samples and the longer the sampling time are, the higher the ADC consumption will be to obtain a single reading from the channel.

To assess the quality of the conversion, the standard deviation of estimator $\overline{V}_R$ was evaluated while varying the parameter M and the sampling period (and maintaining $N=250$, which represents the lowest number of samples that can be read in a single-shot acquisition) in the range $16 \cdot ADC_{\text{clock period}} < ADC_{\text{SamplingPeriod}} < 192 \cdot ADC_{\text{clock period}}$, where $ADC_{\text{clock freq}} = 16$ MHz.

The best trade-off between power consumption and quality of averaged reading $\overline{V}_R$ was found for M = 10 and $ADC_{\text{SamplingPeriod}} = 96$ $ADC_{\text{clock period}}$. Indeed, with this configuration the standard deviation of the estimator of (2) is equal to 0.02 LSB, thus negligible compared to the other sources of uncertainty in the channel.
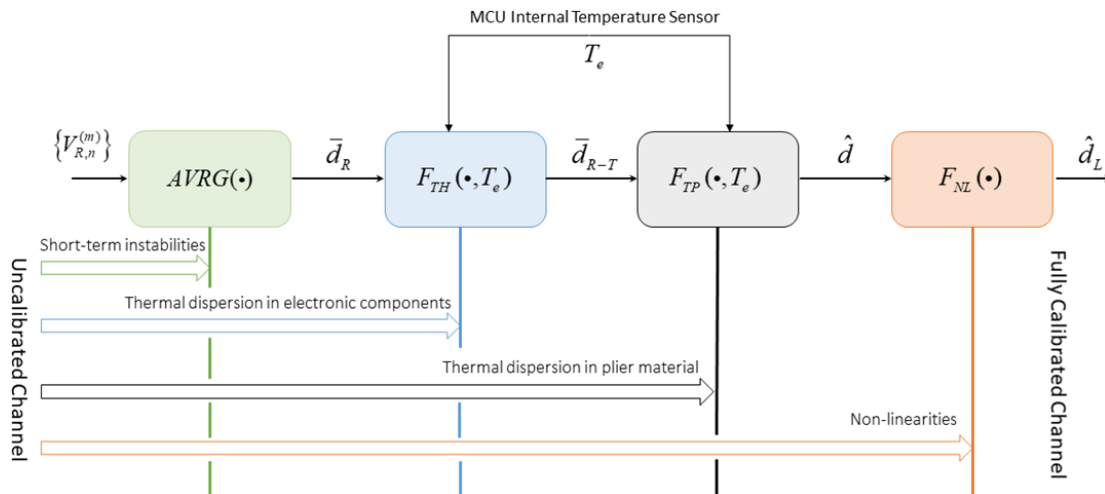

Figure 5. Stages of the overall real-time calibration procedure implemented for each channel in the prototype

4.2. Compensation for thermal dispersion

A climatic chamber has been exploited to carry out an extensive experimental investigation on the dispersion of the prototype sensor-node channel response for temperature variations in the interval 20 °C - 70 °C. During each test, only some parts of the sensor-node were exposed to the temperature cycles, while all the other blocks were kept in constant environment conditions, in order to separately characterize the sources of uncertainty due to thermal variations. These tests included thermal cycles on the NUCLEO64 board (i.e., affecting mainly the ADC and the reference voltage generator), the potentiometers, and the ABS pliers. Final tests were then performed on the entire multi-channel system.

As far as the potentiometers are concerned, no significant thermal dispersion was observed, except for some very small variations probably caused by thermal inertia. ADC and ref voltage generator showed instead, as expected, a significant dispersion, even though the dispersion of the ADC V_{ref} is inherently compensated, at least for the most part, by the adopted strategy of using it to also supply the potentiometers.

For a given sensing channel, $\bar{d}_R$ is defined as the estimator obtained by inserting $\overline{V_R}$ as the ADC averaged reading for V_{out} into (1). The dispersion of $\bar{d}_R$ due to temperature variations affecting the ADC, the ref voltage generator and, from a general standpoint, all the electronic hardware on the boards has been found through the tests to follow the model:

$$\bar{d}_R = \bar{d}_R^{(0)}(1 + C_{th} \cdot \Delta T) \qquad (3)$$

where
- ΔT is the variation of the temperature estimated by the MCU internal sensor with respect to a reference $T^{(0)} = 25$ °C,
- $\bar{d}_R^{(0)}$ is the value of the estimator at $T^{(0)}$ and
- C_{th} is an experimentally estimated temperature coefficient characterizing the channel.

Thanks to the adoption of the already mentioned ref voltage supply strategy, the power gating method described in Subsection 3.7, and an accurate optimization in the design of the entire system, C_{th} has been found adequately independent from temperature and aperture for a given channel. Regarding the power gating, more precisely, an effective solution was to use low Rds_{on} external PMOS (207 mΩ at 27.5 °C) as switches. Rds_{on} variation of these PMOS, estimated using Spice simulation, is equal to 11.9 mΩ over a temperature range between 15 °C and 50 °C. This variation has negligible effects on the final measurement: in the worst case the maximum difference in supply voltage at the potentiometers is 7.9 µV, while the quantization step of the ADC is 806 µV.

The experimental extraction of the coefficient C_{th} for each sensing channel was carried out by obtaining $\bar{d}_R$ on a set of aperture values from a minimum up to the full-scale, applying for each aperture value an entire temperature cycle. During a cycle, the clamp was kept mechanically blocked to the test aperture, so that to not involve in the dispersion of $\bar{d}_R$ the thermal expansion of ABS (see next Subsection). The data collected allowed to write, by means of (3), an overdetermined system of linear equations, whose solution (least-square method) provided the temperature coefficient for the channel under test. An example of temperature cycle applied to the five sensing channels for the test aperture value $d \cong 9$ cm is reported in Figure 6 and Table 1. A weak thermal inertia effect was recorded in some tests, due to
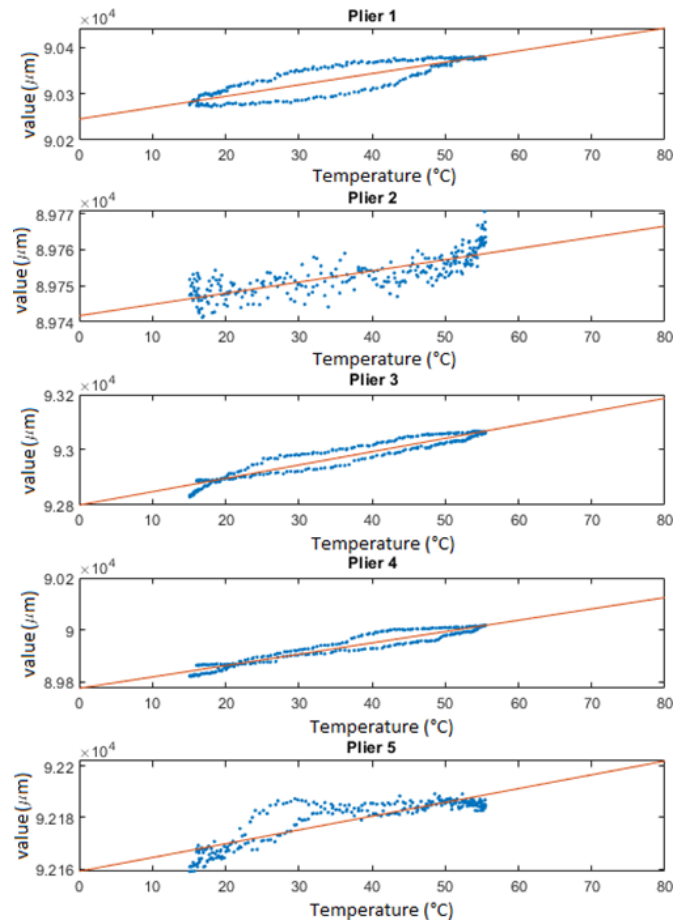

Figure 6. Temperature cycles imposed to the overall final prototype, equipped with PMOS instead of MIC5365-3.3 LDO, for all the five sensing elements.

the need of speeding up the cycle: however, this effect did not cause any major issue during the calibration phase since the resulting pattern is, in almost all cases, symmetrical to the interpolation line and because the points are almost superimposable on the line once thermal equilibrium is reached. It is worth noting that in on-field applications, temperature slope is never so high, thus avoiding thermal inertia.

Once the estimate for the coefficient C_{th} is available for every channel, (3) can be used to convert (according to the model and the assumptions discussed) the uncalibrated averaged reading $\overline{d}_R$ obtained at temperature T_e (monitored by the MCU internal sensor) into the value that would be obtained at the reference $T^{(0)}$. This thermally-calibrated estimate is indicated as $\overline{d}_{R-T}$ in the following.

Table 1. C_{th} and R^2 values, starting with sensing element num. 1 up to sensing element num. 5. Coefficients of the regression lines are computed by means of the least-squared method.

Channel	C_{th}	R^2
1	-0.29	0.776
2	-0.0362	0.641
3	-0.55	0.913
4	-0.51	0.925
5	-0.061	0.754

4.3. Thermal expansion of the pliers

The material used to manufacture the pliers, namely ABS, has a known coefficient of linear expansion λ. Therefore it is possible to estimate, given a reference length $R^{(0)}$ at a reference temperature $T^{(0)}$, and knowing the temperature variation ΔT from the latter, the variation of effective length ΔR of the clamp arm and, consequently, rewrite (1) in the following form

$$d = d^{(0)} + 2 \cdot \Delta R \cdot \cos\left(\frac{\pi}{2} - \frac{\alpha(V_{\text{out}})}{2}\right) \qquad (4)$$

The calibration of all electronic components with respect to thermal dispersion discussed in the previous Subsection can be thus supplemented with the calibration for thermal expansion of the pliers: it suffices to rewrite and estimate (4) in the form:

$$\hat{d} = \overline{d}_{R-T} + 2 \cdot \Delta R \cdot \cos\left(\frac{\pi}{2} - \frac{\alpha(\overline{V}_R)}{2}\right) \qquad (5)$$

to obtain an estimate $\hat{d}$ fully compensated in temperature.

4.4. Non-linearities calibration

Up to now, issues associated with system nonlinearities (ADC nonlinearity, potentiometer resistive taper nonlinearity, geometric dispersion in pliers printing process, etc.) that may affect the $\hat{d}$ estimator have not been addressed. In order to complete the real-time calibration process, it is only required to extract a single calibration curve across the entire measuring range, at constant temperature ($T^{(0)} = 25\,°C$ in this specific example), using a precision reference caliber. By means of a cubic spline interpolation process a set of coefficients is extracted from this curve and saved in the memory of the MCU. At each query on the diameter of the fruit these coefficients are recalled and the linearized output $\widehat{d_L}$ (i.e., the final reading of the channel) is computed from $\hat{d}$ in real time.

A special-purpose laboratory set-up was arranged to calibrate the opening of the pliers. All the pliers of a single node are installed on a structure constrained to the carriage of a CNC. As the carriage moves, it allows the pliers to be opened according to user-defined dimensions, simulating the presence of a fruit of known size. A specially developed Matlab script allows the entire opening range of the pliers to be swept at known spatial intervals, while at the same time the opening value detected in the absence of calibration are acquired. The point couples detected in this way are automatically stored into the flash memory of the microcontroller, thus completing the non-linearity calibration process. In this way each node can be programmed with the same firmware, without the need to modify the code according to the set of calibration coefficients needed for each set of pliers.

5. EXPERIMENTAL RESULTS AND IN-FIELD TESTS

5.1. Static tests

A set of static tests were performed on the prototype sensing channels at room temperature in order to estimate the effective resolution obtained. During the tests, estimates $\widehat{d_L}$ on sets of aperture points randomly distributed within the full range were collected and compared with the readings taken with a precision caliper adopted as reference. By means of simple algorithms the rms deviation was estimated, leading to a standard uncertainty corresponding to 70 μm. Based on this value, the average effective quantisation step $d_q \cong 250$ μm was derived, and ENOB = 9.0 bit estimated for a full-scale range of 12 cm.

5.2. In-field test

A first trial was conducted between June and August 2021, in an apple orchard (Malus x domestica Borkh., cv "Fuji-Fujiko") of the experimental farm of the Department of Agricultural and Food Science of University of Bologna (Cadriano, 44.5543 N - 11.41872 E, Figure 7). The orchard, established in early 2019 in a deep silt-clay soil, was characterized by orchard row spacing of 2 m and tree spacing of 3 m. Trees, grafted onto M9 rootstock and trained to a multi-axis system (10 axis/tree) with a N- S orientation, are watered by means of an irrigation system consisted of drip irrigation with a distance between emitters of 0.5 m and emitter flow of 2.3 Lh⁻¹. Commercial practices, such as manual fruit thinning to achieve optimal crop load, winter pruning to maintain the desired training system, mineral fertilization, pest control and diseases, herbicide application below trees and mowing of inter-canopy cover crop, are employed to manage the orchard.

Within the orchard 18 fruits, randomly selected along a whole row at the beginning of the season, were monitored cyclically and their growth measured by hand using gauges. The five pliers of the prototype were instead placed simultaneously on a different set of five fruits of two adjacent trees, located at about one third of the length of the orchard, in an inner row. Measurements $\widehat{d_L}$ by means of the prototype were performed automatically every 10 minutes, while manual readings were carried out depending on the weather conditions and the activities to be done in the field, without any pre- scheduled periodicity, according to a traditional approach. Such a short time interval between two acquisitions was decided because one of the purposes of the device is to evaluate the variation in fruit size between day and night. This time interval obviously can have an impact in terms of amount of data transmitted or stored. However, it would be straightforward to vary the data acquisition rate according to different, specific needs.

In-field results of the five sensing elements can be seen in Figure 8.

As can be noted in the graph, three sensing elements (i.e., #1, #2 and #4, left) out of five correctly monitored and recorded (apart from recoverable perturbations) the fruit growth throughout the ripening season without the need for any
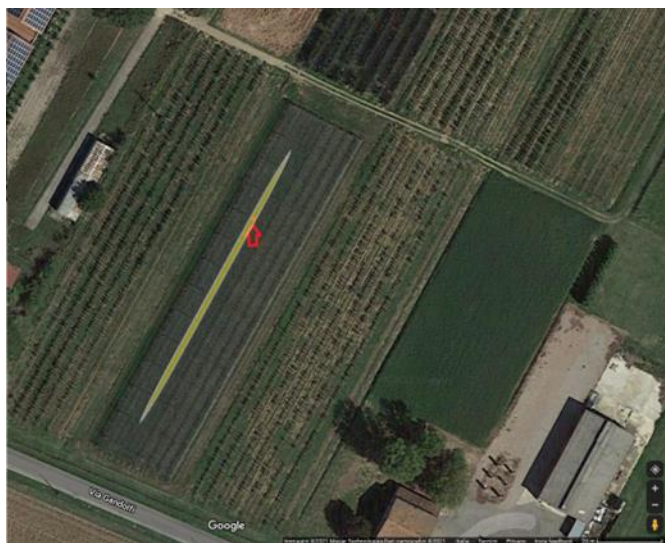

Figure 7. Position of the five pliers of the prototype within the orchard (red dot), and position of the 18 apples manually measured as reference (yellow box).
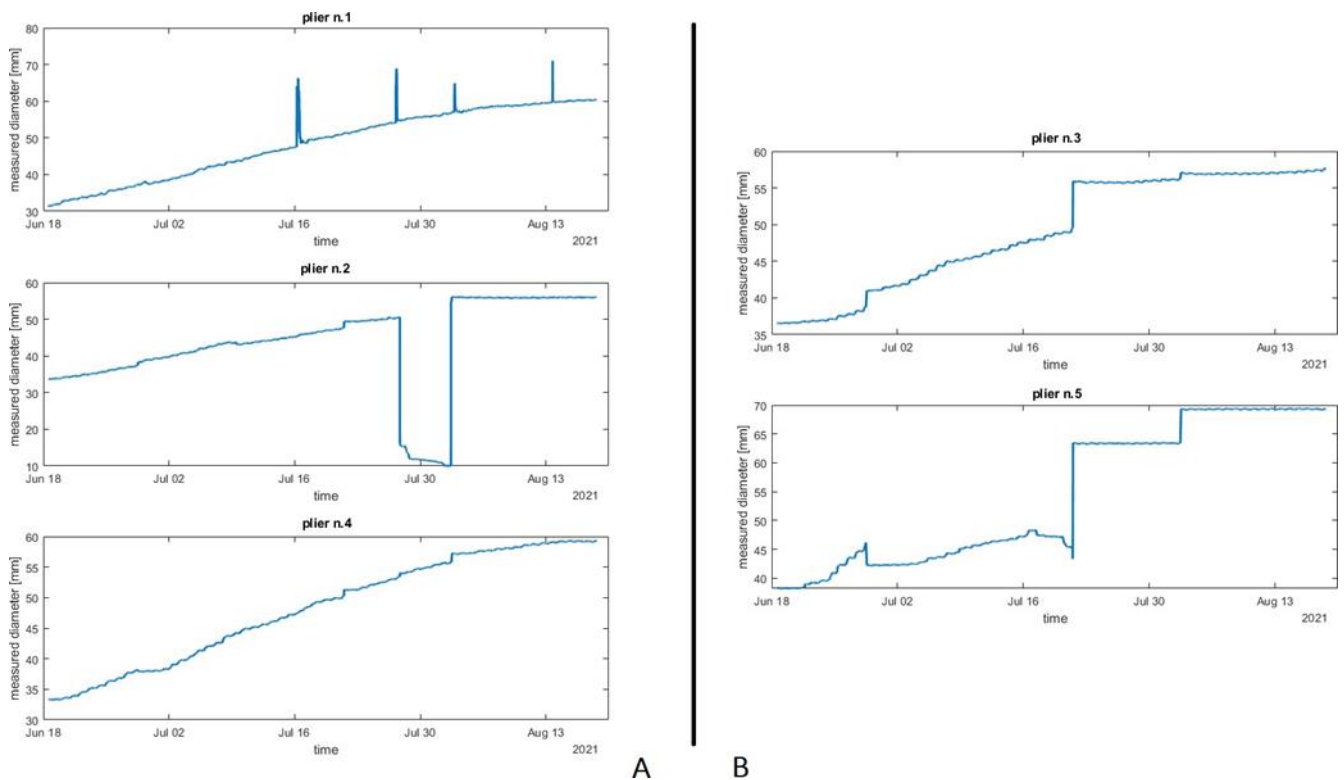
Figure 8. Data acquired by the five sensing-element fully calibrated prototype during the in-field test in the apple orchard at the experimental farm of the Department of Agriculture and Food Sciences of University of Bologna between June and August 2021. On the left (A), successful records that show a correct growth rate and that are not characterized by unrecoverable spikes or disturbances are shown. On the right (B), records that were not useful for this study, due to unrecoverable disturbances (i.e., the clamps suffered from shifts on the fruit due to either weathering or manual activities), are shown.

manning (apart from a single event, detailed below), while sensing elements #3 and #5 (right) suffered from unrecoverable issues. These were not related to the performance of the prototype itself, but to the capability of the pliers to remain reliably fixed to the fruit without any shift in position: normal manual activities, such as pruning the trees or applying spray treatments, or particularly adverse weather conditions, can actually result in a shifting of the pliers. These two records will therefore be disregarded. In the case of sensing element #1, instead, the spikes observed are caused by non-disruptive, recoverable manual activities around the fruit, and can be easily filtered out by software post-processing, while in sensing element #2 the single discontinuity observed at the turn of the 30th of July was caused by strong winds, which caused the sensor to be detached from the fruit. In this case, a manual re-positioning was needed. Such a macroscopic issue can be successfully dealt with by fast visual inspection on the fruits under test, and the exceptionality of the event still allows to state that the monitoring process required a practically negligible work overhead from the orchard staff during the whole ripening season.

Due to the difficulty of obtaining repeatable reference measurements on fruits still attached to the tree (the non-sphericity and non-rigidity of the apple makes it practically impossible to get perfectly repeatable measurements by manual gauges), in order to perform a comparative analysis with the results from the prototype the absolute growth rate (AGR), expressed in mm/day and computed on intervals of several days, was used as an averaged estimator for comparisons. The duration of the intervals over which the AGR was estimated is not constant but depends on the weather conditions and on the other activities required in the field according to common practices. Firstly, the average AGR from the gauge measurements was computed for each individual fruit in the row (see in Figure 9 the statistical distribution obtained) over the total time of the trial (starting from 21/06/2021 to 06/08/2021).

Similarly, the average AGR involving all fruits was calculated on each time interval considered. The same was done, for the same time intervals, by averaging the values obtained with sensing elements #1, #2 and #4 (Table 2).

The values of Table 2 have been graphed in Figure 10, where it is possible to appreciate that the trends of the data collected by

Table 2. From left to right: average AGR values computed, over three time intervals, considering prototype sensing elements 1-4, 1-2-4 and all 18 hand-measured fruits, respectively.

Time interval	AGR 1-4 in mm/day	AGR 1-2-4 in mm/day	AGR gauges in mm/day
21/06/2021 - 08/07/2021	0,56	0,55	0,41
08/07/2021 - 23/07/2021	0,58	0,52	0,41
23/07/2021 - 06/08/2021	0,43	0,44	0,29

Table 3. AGR estimated over the whole duration of the test considering sensing elements 1-4, 1-2-4 and all hand-measured fruits using a gauge.

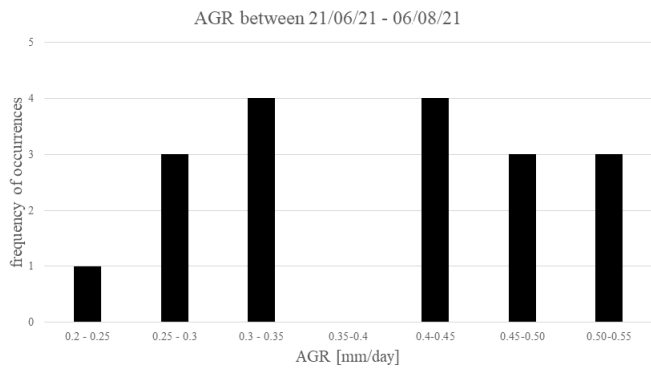| Time interval	AGR in mm/day	deviation in %
21/06/21-06/08/21 | pliers 1-4	0,53	36
21/06/21-06/08/21 | pliers 1-2-4	0,51	31
21/06/21-06/08/21 | gauges	0,39	-

Figure 9. AGR distribution of all the 18 apples manually measured, computed over the total time of the trial.
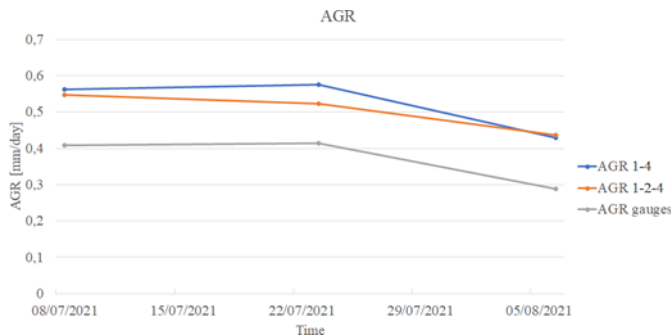

Figure 10. Comparison between averaged AGR computed with data collected by the prototype sensing elements and reference data collected with manual caliper.

the sensing elements and the hand-measured readings are very close.
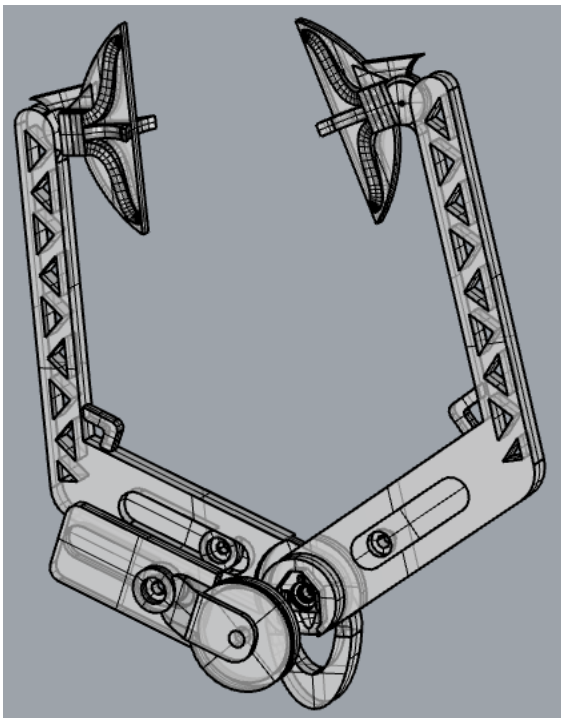

Figure 11. New plier rendering. It can be seen that the structure has been lightened and the cut-out for the potentiometer has been included into the right-hand body of the plier. The spring is not shown.
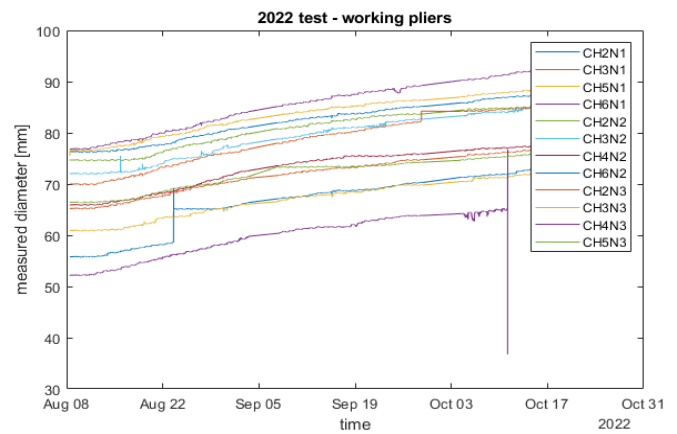

Figure 12. Measured diameter of apples on 2022 test. Only working pliers are shown.

Table 3 reports the comparison between the AGR estimated by the sensor-node prototype throughout the ripening season and the corresponding value from the reference manual readings. On average, the prototype value is slightly higher than the manually measured one. However, looking at the histogram in Figure 9, it can be appreciated that the AGR from the sensing elements, which are positioned on the fruits of two adjacent trees and, thus, is representative of a local sampling of growth rate, is nonetheless within the statistics of the events detected on a larger scale in the orchard, i.e., an entire row. According to these results, and by considering the statistical distribution in Figure 9, 4-5 equally-spaced sensor-nodes could suffice for an adequate sampling of fruit growth along an entire row with these characteristics.

A further test was performed using 3 nodes, each consisting of 5 pliers, between August 2022 and October 2022. The orchard was the same of the first test and sensor nodes were randomly distributed over nonadjacent trees on the same row where previous year's test was conducted. Sensor-nodes, whose pliers were shared between adjacent trees, were programmed with same settings as the one used in the previous year's test. Thanks to the experience gained with the tests of the previous year, this campaign was performed with a new version of the pliers. Structural changes in the shape were introduced in order to lighten it, to improve its adhesion to the fruit and to simplify the 3D printing process while minimising production tolerances. (Figure 11) The average of the AGR factor estimated using these devices was compared to the average of the same factor computed on 22 hand measured fruits, randomly selected, of the same orchard. Of 15 total pliers, only 3 revealed problems with slipping on the fruit. The values measured by these pliers will therefore not be considered for the calculation of the AGR. The remaining 12 channels all show approximately the same growth trend (Figure 12).

Thanks to the new design of the pliers, a more accurate positioning of them on the fruits made it possible to decrease the number of required relocations, making the measurements less perturbed than in the previous test. In fact, significant spikes are no longer present in the acquisitions (Figure 12).

For AGR determination, manually acquired data were collected on different dates, selected according to weather conditions and field operations. Therefore, two time intervals were obtained within which the AGR was computed (Table 4). These values were compared with the ones obtained from the data acquired with the multi-channel sensor-nodes. In this case,

Table 4. Average AGR values of hand measured fruits computed, over two times intervals in 2022 test, with a gauge.

Time interval - manual acquisition	AGR in mm/day
01/08/2022 - 30/08/2022	0,34
30/08/2022 - 03/10/2022	0,20

Table 5. Average AGR values of fruits, estimated with the sensor node, over two time intervals during 2022 test, and deviation from AGR computed on hand measured fruits.

Time interval - prototype acquisition	AGR in mm/day	deviation in %
18/08/2022 - 30/08/2022	0,33	-2
30/08/2022 - 04/10/2022	0,17	-16

it was not considered useful to perform an analysis of the statistical distribution of AGR between fruits as this had already been done in the past experimental campaign, but rather to verify the validity of the measurement with a statistically representative number of samples representing the conditions of the entire orchard. Results are shown in Table 5.

The time intervals considered for calculating AGR factor using hand gauges are different from those considered for calculating the same parameter with our devices. This, however, is not a source of error since growth pattern of an apple follows different phenological stages, each characterised by a typical growth profile. Therefore, while remaining within each phenological phase, the AGR value is approximately the same. In particular, periods 01/08/2022 - 30/08/2022, considered for the manual acquisition, and 18/08/2022 - 30/08/2022, used for estimation of AGR with our system, belong to the same phenological phase and can therefore be compared without appreciable errors.

The delay in the start of the comparison is caused by the need for the pliers to adapt to mechanical clearances. In fact, looking at Figure 12, it can be seen how the growth in the first few days seems to be extremely slow, which is not the actual case. In the two time periods, the AGR value is very similar experimentally confirming the good performance of the device.

6. CONCLUSIONS

In this paper, a multi-channel sensor-node architecture and related calibration procedure for continuous distributed monitoring of fruit growth were presented. The low-cost prototype implemented for validation purposes, which was realized by means of commercial boards and 3D-printed devices, showed nonetheless adequately high effective resolution with a full-scale range suitable for no-manning operation throughout the entire ripening season of apple-sized fruit species. By adopting a multi-step calibration procedure, it was possible to compensate each channel in real-time for temperature dispersion, noise and non-linearity, which made the system rugged to environmental conditions and suitable for all-season operation. Thanks to the energy harvesting sub-system and the possibility of data transmission in real-time over the air, the sensor-node and its sensing elements can be positioned at the beginning of the season and operate, without any maintenance required, until harvest time. The design of a custom board is planned, in order to integrate the harvesting stage, the MCU and the LoRa transceiver for performance and power consumption optimization.

REFERENCES

[1] F. J. Pierce, P. Nowak, Aspects of precision agriculture, ser. Advances in Agronomy, D. L. Sparks, Ed. Academic Press, 1999, vol. 67, pp. 1–85.
DOI: 10.1016/S0065-2113(08)60513-1

[2] R. Khan, M. Zakarya, V. Balasubramanian, M. A. Jan, V. G. Menon, Smart sensing-enabled decision support system for water scheduling in orange orchard, IEEE Sensors Journal, vol. 21, no. 16, 2021, pp. 17492– 17499.
DOI: 10.1109/JSEN.2020.3012511

[3] N. Zhang, M. Wang, N. Wang, Precision agriculture - a worldwide overview, Computers and Electronics in Agriculture, vol. 36, no. 2, 2002, pp. 113–132.
DOI: 10.1016/S0168-1699(02)00096-0

[4] B.-Y. Ooi, S. Shirmohammadi, The potential of IoT for instrumentation and measurement, IEEE Instrumentation & Measurement Magazine, vol. 23, no. 3, 2020, pp. 21–26.
DOI: 10.1109/MIM.2020.9082794

[5] D. Davcev, K. Mitreski, S. Trajkovic, V. Nikolovski, N. Koteli, IoT agriculture system based on LoRaWan, 2018 14th IEEE International Workshop on Factory Communication Systems (WFCS), Imperia, Italy, 13-15 June 2018, pp. 1–4.
DOI: 10.1109/WFCS.2018.8402368

[6] M. J. Faber, K. M. van der Zwaag, W. G. V. dos Santos, H. R.d. O. Rocha, M. E. V. Segatto, J. A. L. Silva, A theoretical and experimental evaluation on the performance of lora technology, IEEE Sensors Journal, vol. 20, no. 16, 2020, pp. 9480–9489.
DOI: 10.1109/JSEN.2020.2987776

[7] M. Reichardt, C. Jürgens, Adoption and future perspective of precision farming in Germany: results of several surveys among different agricultural target groups, Precision agriculture, vol. 10, no. 1, 2009, pp. 73– 94.
DOI: 10.1007/s11119-008-9101-1

[8] M. Kernecker, A. Knierim, A. Wurbs, Common framework on innovation processes and farmers' interests. Online [Accessed 2 June 2023]
https://ec.europa.eu/research/participants/documents/downloadPublic?documentIds=080166e5a96e5296&appId=PPGMS

[9] A. Lakso, L. Corelli Grappadelli, J. Barnard, M. Goffinet, An expolinear model of the growth pattern of the apple fruit, Journal of Horticultural Science, vol. 70, no. 3, 1995, pp. 389–394.
DOI: 10.1080/14620316.1995.11515308

[10] H. Welte, Forecasting harvest fruit size during the growing season, Acta Horticulturae 276: II Int. Symposium on Computer Modelling in Fruit Research and Orchard Management 276, 1989, pp. 275–282.
DOI: 10.17660/ActaHortic.1990.276.32

[11] B. Morandi, F. Boselli, A. Boini, L. Manfrini, L. Corelli, The fruit as a potential indicator of plant water status in apple, Acta Horticulturae: VIII Int. Symposium on Irrigation of Horticultural Crops 1150, 2017, pp. 83–90.
DOI: 10.17660/ActaHortic.2017.1150.12

[12] A. Boini, L. Manfrini, G. Bortolotti, L. Corelli-Grappadelli, B. Morandi, Monitoring fruit daily growth indicates the onset of mild drought stress in apple, Scientia Horticulturae, vol. 256, 2019, p. 108520
DOI: 10.1016/j.scienta.2019.05.047

[13] S. O. Link, M. E. Thiede, M. G. v. Bavel, An improved strain-gauge device for continuous field measurement of stem and fruit diameter, Journal of Experimental Botany, vol. 49, no. 326, 1998, pp. 1583–1587.
DOI: 10.1093/jexbot/49.326.1583

[14] B. Morandi, L. Manfrini, M. Zibordi, M. Noferini, G. Fiori, L. C. Grappadelli, A low-cost device for accurate and continuous measurements of fruit diameter, HortScience, vol. 42, no. 6, 2007, pp. 1380– 1382.
DOI: 10.21273/HORTSCI.42.6.1380

[15] M. Thalheimer, A new optoelectronic sensor for monitoring fruit or stem radial growth, Computers and Electronics in Agriculture,

vol. 123, 2016, pp. 149–153.
DOI: 10.1016/j.compag.2016.02.028

[16] C. Nandi, B. Tudu, C. Koley, Machine Vision Based Techniques for Automatic Mango Fruit Sorting and Grading Based on Maturity Level and Size Maturity Level and Size, In: Mason, A., Mukhopadhyay, S., Jayasundera, K., Bhattacharyya, N. (eds) Sensing Technology: Current Status and Future Trends II. Smart Sensors, Measurement and Instrumentation, vol. 8, 2014.
DOI: 10.1007/978-3-319-02315-1_2

[17] D. Shadrin, A. Menshchikov, A. Somov, G. Bornemann, J. Hauslage, M. Fedorov, Enabling precision agriculture through embedded sensing with artificial intelligence, IEEE Transactions on Instrumentation and Measurement, vol. 69, no. 7, 2020, pp. 4103–4113.
DOI: 10.1109/TIM.2019.2947125

[18] D. Wang, C. Li, H. Song, H. Xiong, C. Liu, D. He, Deep learning approach for apple edge detection to remotely monitor apple growth in orchards, IEEE Access, vol. 8, 2020, pp. 26911–26925.
DOI: 10.1109/ACCESS.2020.2971524

[19] D. Stajnko, M. Lakota, M. Hočevar, Estimation of number and diameter of apple fruits in an orchard during the growing season by thermal imaging, Computers and Electronics in Agriculture, vol. 42, no. 1, 2004, pp. 31–42.
DOI: 10.1016/S0168-1699(03)00086-3

[20] Z. Wang, K. Walsh, B. Verma, On-tree mango fruit size estimation using rgb-d images, Sensors, vol. 17, 11 2017, p. 2738.
DOI: 10.3390/s17122738

[21] K. Bresilla, G. D. Perulli, A. Boini, B. Morandi, L. Corelli Grappadelli, L. Manfrini, Single-shot convolution neural networks for real-time fruit detection within the tree, Frontiers in plant science, vol. 10, 2019, p. 611.
DOI: 10.1088/0031-9120/30/5/007

[22] F. Rossi, L. Manfrini, M. Venturi, L. Corelli Grappadelli, B. Morandi, Fruit transpiration drives interspecific variability in fruit growth strategies, Horticulture Research 9, 2022, pp. 1–10.
DOI: 10.1093/hr/uhac036

[23] L. M. Peppi, M. Zauli, L. Manfrini, L. C. Grappadelli, L. De Marchi, P. A. Traverso, Implementation and calibration of a low-cost sensor node for high-resolution, continuous and no-manning recording of fruit growth, 2021 IEEE Int. Instrumentation and Measurement Technology Conference (I2MTC), Glasgow, United Kingdom, 17-20 May 2021, pp. 1–6.
DOI: 10.1109/I2MTC50364.2021.9459851

[24] TT Electronics, Rotary Position Sensor PHS11 Series. Online [Accessed 2 June 2023]
https://www.ttelectronics.com/TTElectronics/media/ProductFiles/Datasheets/PHS11.pdf

[25] STMicroelectronics, UM1724 User manual. Online [Accessed 2 June 2023]
https://www.st.com/resource/en/user_manual/um1724-stm32-nucleo64-boards-mb1136-stmicroelectronics.pdf

[26] STMicroelectronics, RM0038 Reference Manual. STM32l100xx, STM32L151xx, STM32L152xx and STM32L162xx advanced Arm-based 32–bit MCUs. Online [Accessed 2 June 2023]
https://www.st.com/resource/en/reference_manual/rm0038-stm32l100xx-stm32l151xx-stm32l152xx-and-stm32l162xx-advanced-armbased-32bit-mcus-stmicroelectronics.pdf

[27] STMicroelectronics, HTS221 Datasheet. Online [Accessed 2 June 2023]
https://www.st.com/resource/en/datasheet/hts221.pdf

[28] STMicroelectronics, LD39050 500 mA low quiescent current and low noise voltage regulator. Online [Accessed 2 June 2023]
https://www.st.com/resource/en/datasheet/ld39050.pdf

[29] Arm Limited, SX1272 mbed Shield. Online [Accessed 2 June 2023]
https://os.mbed.com/components/SX1272MB2xAS/

[30] Semtech, SX1272 datasheet. Online [Accessed 2 June 2023]
https://www.semtech.com/products/wireless-rf/lora-core/sx1272#download-resources

[31] Gough's Tech Zone, microSD Card Power Consumption & SPI Performance. Online [Accessed 2 June 2023]
https://goughlui.com/2021/02/27/experiment-microsd-card-power-consumption-spi-performance/

[32] C. Pratt, Apple flower and fruit: morphology and anatomy, Horticultural Reviews, vol. 10, 2011, pp. 273–308.
DOI: 10.1002/9781118060834.ch8

[33] R. W. Porto, V. J. Brusamarello, I. Müller, F. L. C. Riano, F. R. De Sousa, Wireless power transfer for contactless instrumentation and measurement, IEEE Instrumentation & Measurement Magazine, vol. 20, no. 4, pp. 49–54, 2017.
DOI: 10.1109/MIM.2017.8006394

[34] STMicroelectronics, STEVAL-ISV012V1, Data brief. Online [Accessed 2 June 2023]
https://www.st.com/resource/en/data_brief/steval-isv012v1.pdf

[35] Diodes Incorporated, DMP2200UDW Dual p-channel enhancement mode MOSFET, Online [Accessed 2 June 2023]
https://www.diodes.com/assets/Datasheets/DMP2200UDW.pdf